Received: December 27, 2018 Revised: May 10, 2019 Accepted: May 11, 2019

(onlinelibrary.wiley.com) DOI: 10.1111/ner.12980

Tissue Temperature Increases by a 10 kHz Spinal Cord Stimulation System: Phantom and Bioheat Model

Adantchede L. Zannou, BE*; Niranjan Khadka, PhD Candidate*; Mohamad FallahRad, MS*; Dennis Q. Truong, PhD Candidate*; Brian H. Kopell, MD†; Marom Bikson, PhD*

Objective: A recently introduced Spinal Cord Stimulation (SCS) system operates at 10 kHz, faster than conventional SCS systems, resulting in significantly more power delivered to tissues. Using a SCS heat phantom and bioheat multi-physics model, we characterized tissue temperature increases by this 10 kHz system. We also evaluated its Implanted Pulse Generator (IPG) output compliance and the role of impedance in temperature increases.

Materials and Methods: The 10 kHz SCS system output was characterized under resistive loads (1–10 KΩ). Separately, fiber optic temperature probes quantified temperature increases (ΔTs) around the SCS lead in specially developed heat phantoms. The role of stimulation Level (1–7; ideal pulse peak-to-peak of 1–7mA) was considered, specifically in the context of stimulation current Root Mean Square (RMS). Data from the heat phantom were verified with the SCS heat-transfer models. A custom high-bandwidth stimulator provided 10 kHz pulses and sinusoidal stimulation for control experiments.

Results: The 10 kHz SCS system delivers 10 kHz biphasic pulses (30-20-30 μs). Voltage compliance was 15.6V. Even below voltage compliance, IPG bandwidth attenuated pulse waveform, limiting applied RMS. Temperature increased supralinearly with stimulation Level in a manner predicted by applied RMS. ΔT increases with Level and impedance until stimulator compliance was reached. Therefore, IPG bandwidth and compliance dampen peak heating. Nonetheless, temperature increases predicted by bioheat multi-physic models ($\Delta T = 0.64^{\circ}$C and 1.42°C respectively at Level 4 and 7 at the cervical segment; $\Delta T = 0.68^{\circ}$C and 1.72°C respectively at Level 4 and 7 at the thoracic spinal cord)–within ranges previously reported to effect neurophysiology.

Conclusions: Heating of spinal tissues by this 10 kHz SCS system theoretically increases quickly with stimulation level and load impedance, while dampened by IPG pulse bandwidth and voltage compliance limitations. If validated in vivo as a mechanism of kHz SCS, bioheat models informed by IPG limitations allow prediction and optimization of temperature changes.

Keywords: Bio-heat Multi-physics FEM, heating, RMS, spinal cord stimulation (SCS)

Conflict of Interest: The City University of New York (CUNY) has IP on neuro-stimulation system and methods with authors, Niranjan Khadka and Marom Bikson as inventors. Marom Bikson has equity in Soterix Medical. Marom Bikson serves on Boston Scientific and GlaxoSmithKline Inc. advisory boards. Brian H. Kopell consults for Medtronic, Abbott, Elekta. The remaining authors have no conflict to disclose.

INTRODUCTION

The mechanisms of kHz (>1 kHz) spinal cord stimulation (SCS) remain under investigation (1,2). Distinct clinical features of kHz stimulation suggest special mechanisms of action (MoA) compared to conventional frequency stimulation (1–7). As a result of the membrane time constant (~1 mS (8,9)), the short pulse duration and time between pulse phases interval (tens of μS) of kHz stimulation limit direct membrane polarization, further supporting a distinct MoA (4,6,7). A decrease in inter-pulse duration with increased frequency (0.1 mS at 10 kHz) necessitates a decrease in pulse duration; but the proportional decrease in pulse duration is less than the increase in frequency, meaning duty cycle increases at kHz stimulation. We previously showed stimulation power increases at kHz waveforms along with joule heat delivered to tissue, a feature called "pulse compression" (10). As joule heat increases, so does the tissue temperature rises (11,12). Here, we directly assess theoretical temperature increase around the Nevro Senza HF10 SCS system lead using heat phantoms and (bio)heat multi-physics models. A detailed characterization of

Address correspondence to: Marom Bikson, PhD, Department of Biomedical Engineering, The City College of New York, New York, NY 10031, USA. Email: bikson@ccny.cuny.edu

* Department of Biomedical Engineering, The City College of New York, New York, NY, USA; and

† Department of Neurosurgery, Neurology, Psychiatry and Neuroscience, The Icahn School of Medicine, Mount Sinai, NY, USA

For more information on author guidelines, an explanation of our peer review process, and conflict of interest informed consent policies, please go to www.wiley.com/WileyCDA/Section/id-301854.html

Source(s) of financial support: This study was partially funded by grants to MB from National Institutes of Health (NIH-NIMH 1R01MH111896, NIH-NINDS 1R01NS101362, NIH-NCI U54CA137788/U54CA132378, R03 NS054783) New York State Department of Health (NYS DOH, DOH01-C31291GG), RISE Graduate Fellowship at CCNY.

Senza IPG output, including bandwidth and compliance limitations, under varied stimulation level and load impedance, was related to IPG output power and maximal temperature rise. Using a custom high band-width benchtop stimulator we assessed whether stimulation RMS, independent of other waveform features, determines heating.

METHODS

Stimulation and Output Analysis

The polyurethane Senza HF10 SCS lead (Nevro Corp., Redwood City, CA, USA) with 8 Platinum/Iridium (Pt/Ir) electrode contacts (E: electrode diameter: 1.3 mm; electrode length: 3.0 mm; edge-to-edge inter-electrode spacing: 4.8 mm) was energized (E1–E2 or E5–E6) for all analysis. Output current of the commercial rechargeable Senza HF10 SCS Implantable Pulse Generator (IPG) (Nevro Corp.) was passed across 1–10 kΩ resistive loads (approximating a per electrode resistance of 0.5–5 kOhm (13–15)); across the electrode contacts of the Senza SCS lead. Separately, a customized in-house linear current stimulator (LCI) driven by a function generator (AFG320, Tektronix, Beaverton, OR, USA) was used to generate either 10 kHz symmetric charge-balanced biphasic pulse waveforms, mimicking the waveform parameters of the Senza HF10 or 10 kHz sinusoidal waves. Across experiments, the 10 kHz waveform (IPG pulses, LCI pulsed, LCI sinusoid) was not varied, only intensities were varied and reported as "Level" or "target current." Stimulation level (Senza IPG program setting) corresponds to nominal peak-to-peak amplitude. The experimental output voltage signals from varied resistive loads and stimulation levels were acquired using a digital mixed signal oscilloscope (MSO2024, Tektronix, OR, USA), analyzed using MATLAB (MathWorks, MA, USA), and were used to calculate the output voltage RMS, the output current RMS (output voltage/resistance), and the output power values. We also confirmed experimental output RMS current also using built in functions of the digital mixed signal oscilloscope (MSO2024), a DAQ (NI PCI 5922, National Instruments, TX, USA), and a digital multimeter (DMM 7510 $7\frac{1}{2}$ Digit Graphical Sampling Multimeter, Tektronix, OR, USA). The current RMS (I_{RMS}) measured at 1 kΩ were considered the "applied RMS" for computational FEM simulation. Stimulation intensities were converted to theoretical RMS intensities ($I_{Th\text{-}RMS}$) values by

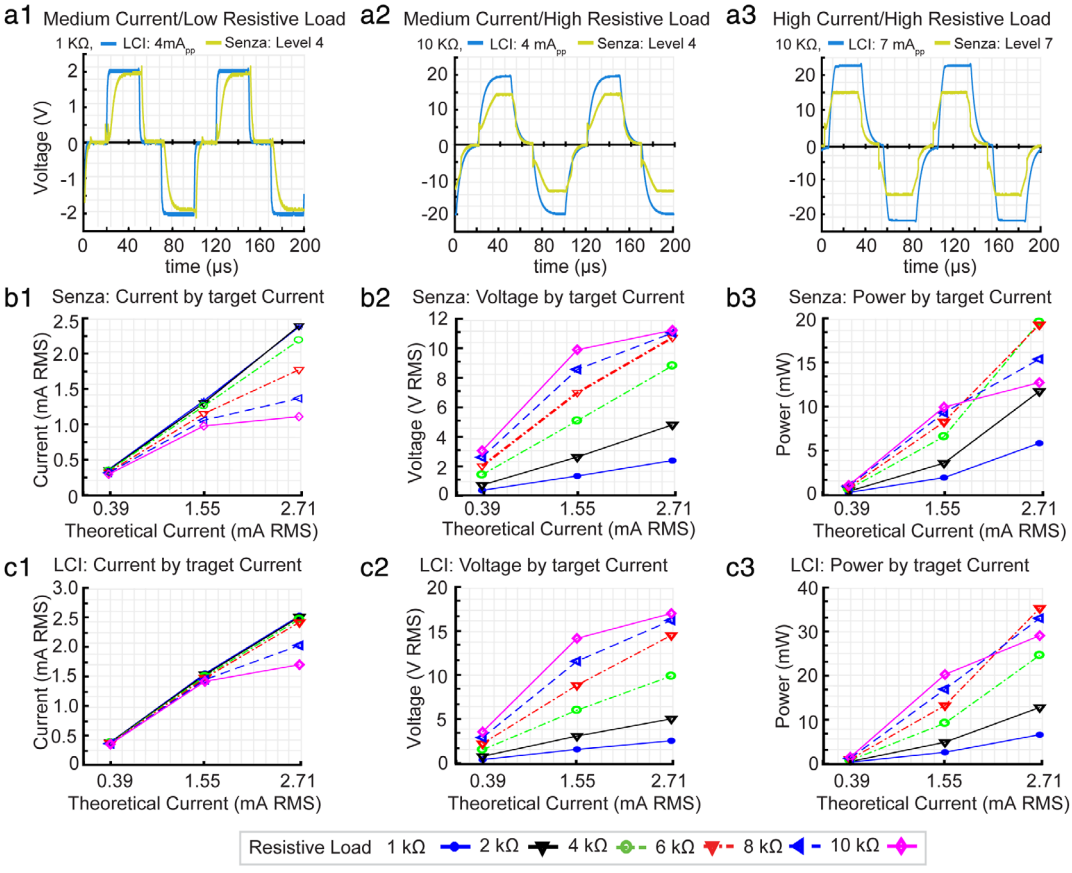

Figure 1. Electrical output performance of Senza HF10 SCS system: bandwidth, compliance, and power limits. The voltage output of the Senza HF10 SCS IPG and of an in-house high-bandwidth LCI current stimulator producing matched target waveform (10 kHz, 30–20–30 μs) were measured across resistive loads. (top row, a) For the Senza (green) and LCI (blue), voltage waveforms for conditions of (a1) mid current (4 mA$_{peak\text{-}to\text{-}peak}$, Level 4) and low resistive load (1 kΩ); (a2) mid current and "high resistive load (10 kΩ); and (a3) high current (7 mA$_{peak\text{-}to\text{-}peak}$, Level 7) and high resistive load (10 kΩ). Note, the ideal target voltages for a1, a2, and a3 conditions were 2 V$_{peak}$, 20 V$_{peak}$, and 35 V$_{peak}$, respectively. (Middle Row, b) Senza IPG electrical output across varied resistive loads (color, 1–10 kΩ) for increasing target current of 1 mA$_{peak\text{-}to\text{-}peak}$/Level 1 (corresponding to a theoretical 0.39 mA RMS), 4 mA$_{peak\text{-}to\text{-}peak}$/Level 4: corresponding to a theoretical 1.55 mA RMS), and 7 mA$_{peak\text{-}to\text{-}peak}$/Level 7 (corresponding to a theoretical RMS 2.72 mA RMS). For each target current, output current RMS (b1), output voltage RMS (b2), and peak power (b3) were measured. (bottom row, c) LCI current stimulator output collected as for the Senza IPG. In each plot, deviation from a linear indicates nonideal performance. Note maximal power (b3, c3) is provided at mid-range resistance values associated with linear current (b1, c1) and sub-compliance limit voltage (b2, c2) responses. [Color figure can be viewed at wileyonlinelibrary.com]

multiplying the theoretical peak stimulation current (I_{Peak} = half of the stimulation level) and the square root of the theoretical duty cycle (60%) as in Equation (1) (10).

$$I_{TH-RMS} = 0.5*level*\sqrt{0.6} \quad (1)$$

For sinusoidal waveforms, the $I_{TH\text{-}RMS(sin)}$ was calculated by multiplying the peak stimulation current by $\frac{\sqrt{2}}{2}$ as:

$$I_{TH-RMS(Sin)} = \frac{\sqrt{2}}{2}*Ipeak \quad (2)$$

Battery Rundown

The Nevro Senza HF10 SCS system battery was fully charged then discharged fully across varied resistive loads (1, 6, or 10 kΩ) with two stimulation intensity levels (4 or 7). The time (sec) until the battery was completely drained ($T_{Drainage}$) was determined for each level-resistive load combination.

We modeled the Senza IPG energy output as baseline power consumption ($P_{Baseline}$, reflecting energy use by the background IPG functions independent of output to leads) and the lead power consumption (P_{Lead}, energy effectively delivered to the body), which are reflected in total energy consumption (E_{Th}) as:

$$E_{Th} = P_{Baseline}*T_{Drainage} + P_{Lead}*T_{Drainage} \quad (3)$$

$P_{Baseline}$ is estimated based on discharge time with minimal P_{lead} (Level 1, 100 Ω). The total energy provided to the lead (E_{lead}) and P_{lead} are calculated from experimentally determined IPG output voltage (see above) as (16–18):

$$E_{Lead} = P_{Lead}*T_{Drainage} = \frac{V^2*pw*f*T_{Drainage}}{R} \quad (4)$$

Heat Phantom Preparation

A phantom gel was prepared by mixing 10 g of laboratory grade Agarose ash (HP34, Caputron, New York, NY) and NaCl (weighted to set phantom conductivity: 0.025 S/m, 0.04 S/m, and 0.085 S/m) into 1 L of deionized water. The mixture was boiled above 90 °C then poured into a phantom mold (cylindrical; h = 150 mm, d = 100 mm). The stimulation lead and temperature probes were positioned in the gel heat phantom as its temperature dropped to ~40°C. The gel was further allowed to cool under the room temperature to finalize the gelation process. The water bath (280 × 160 × 150 mm^3) temperature controller was set to 37°C and the phantom was placed into the bath for ~ 12 hours to attain equilibrium temperature (Fig. 2a). The electrical and thermal conductivities of the phantom were verified using Conductivity Benchtop Meter (Orion™ Star A212, Thermo Fisher Scientific Inc., Waltham, MA, USA) and Thermal properties analyzer (KD2 Pro, Decagon Devices Inc., Pullman WA, USA), respectively.

Phantom Stimulation and Temperature Measurement

The Senza SCS IPG or LCI was connected to the SCS lead positioned at the center of the phantom (Fig. 2a) and programmed using a remote controller. All tested montages were adjacent bipolar electrode contacts (E1–E2; E5–E6). Tested stimulation intensities were Level 1–7 corresponding to 1–7 $mA_{peak\text{-}to\text{-}peak}$. A fiber optic temperature probe (STS Probe Kit, LumaSense Technologies, Inc. CA, USA) sensed by a fiber optic thermometer (±0.1°C accuracy at calibration temperature, FOT LAB KIT, LumaSense Technology, CA, USA) was positioned proximal to the E6 (~0.5 mm radially away from the

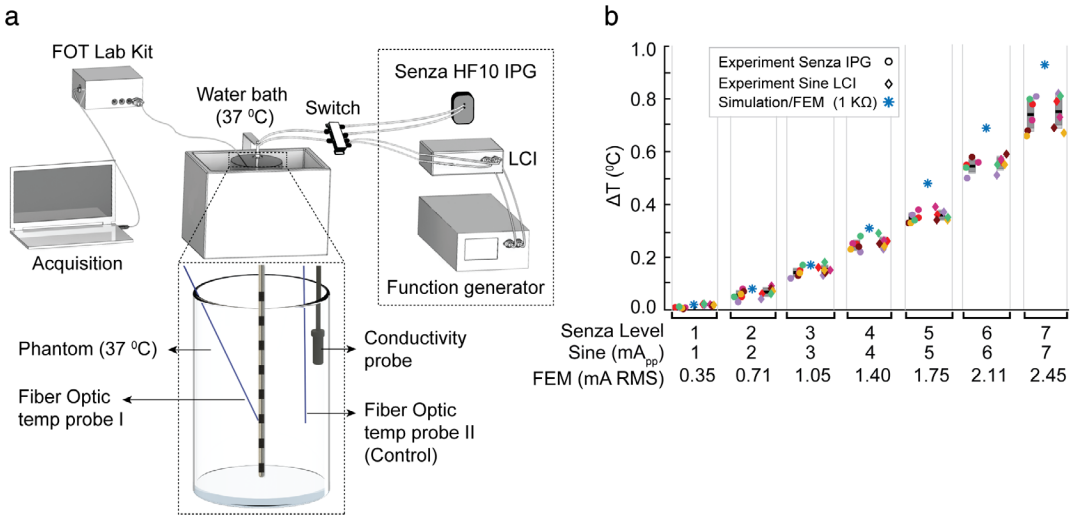

Figure 2. Significant temperature increases in a heat phantom during Senza HF10 SCS stimulation. a. Schematics (not drawn to scale) of heat phantom experimental setup with a Senza SCS lead in the HP34 agarose gel phantom, function generator driving custom LCI stimulator or Senza IPG energizing the SCS lead (at electrodes E5–E6), conductivity probe, and FOT Lab kit temperature sensor hardware and software with optical temperature probe mounted on a micromanipulator. b. In a medium conductivity phantom (0.04 S/m), ΔT measured (sensor coverage ~1 mm radial from E) around electrode E6 when activating the Senza IPG or a 10 kHz sine wave through the LCI stimulator with output intensity varied corresponding to 0.35, 0.7, 1.05, 1.4, 1.75, 2.1, and 2.45 mA RMS. For matched RMS, ΔT by the IPG (10 kHz pulses) or LCI (10 kHz sinusoidal) were not significantly different. ΔT was predicted in the bioheat SCS model at 0.5 mm from E6. ΔT increased with stimulation intensities in both experiment and FEM study. Maximum temperature measured experimentally and predicted computationally approached 1°C at 1 mm from electrode in the medium conductivity (0.04 S/m) phantom. Percent differences between FEM predicted ΔTs and the experimental ΔTs for Level 1–7 are 1.2, 2.3, 2.8, 6.5, 13.2, 14.5, and 18.8% and 1.2, 2.1, 3.1, 5.3, 13.3, 13.7, and 17.5%, respectively, for Senza IPG and LCI. [Color figure can be viewed at wileyonlinelibrary.com]

electrode midline) to measure the temperature increases during stimulation. Measured temperature was digitized using TrueTemp data acquisition and graphing software (60 samples/measurement and 1 sec measurement interval, LumaSense Technologies, Inc. CA, USA). Temperature was normalized with respect to the initial temperature (~37°C), also considered as the baseline temperature.

Model Construction and Computation Method

Computer-aided design (CAD) model of the phantom and human spinal cord with SCS lead and temperature probes were designed and assembled in SolidWorks 2016 (Dassault Systemes Americas Corp., MA, USA), and imported in Simpleware ScanIP (Synopsys Inc., CA, USA) for segmentation and mesh generation. The FEM Phantom model was parametrized based on the dimensions, SCS lead positioning, conductivities, and initial temperature of the experimental setup. We modeled high resolution (~0.15 mm) lower thoracic (T8–T12) and cervical level (C3–C6) spinal cord model with seven tissue compartments namely vertebrae, intervertebral disc, soft-tissues, epidural space, dura, CSF, and spinal cord (white matter and gray matter combined) (Fig. 3). The assigned dimensions for the tissues were based on human cadaveric spinal cord from previous studies (16,17). An adaptive tetrahedral mesh was generated using voxel-based meshing algorithms of ScanIP. The FE model meshes resulting from

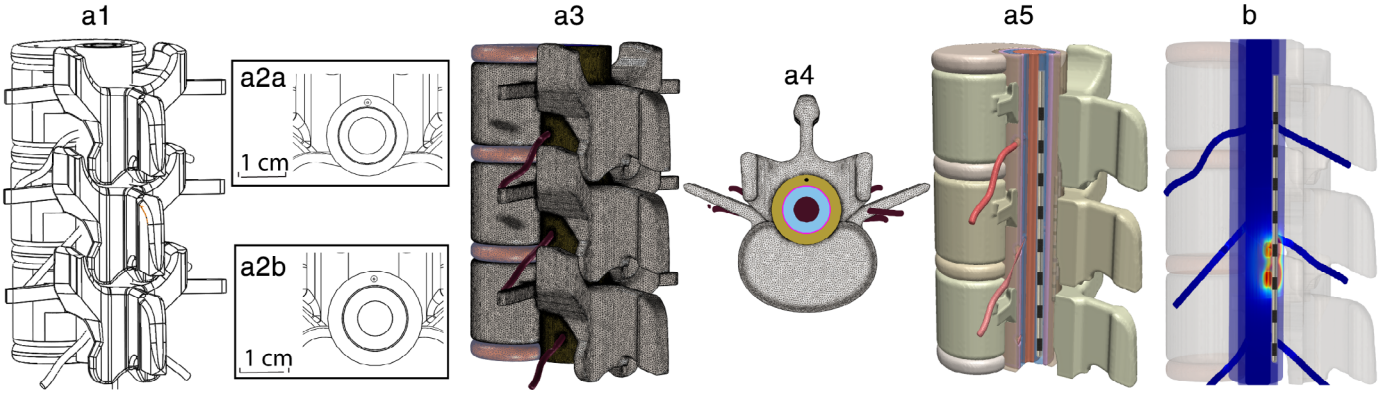

e1

Intensity		ΔT (°C)		EF (V/m)	
Level	RMS (mA)	Lead	SC	Lead	SC
1	0.35	0.03	0.02	700	7
2	0.70	0.12	0.05	1400	13
3	1.05	0.28	0.09	2100	20
4	1.40	0.50	0.15	2780	26
5	1.75	0.78	0.24	3470	33
6	2.10	1.12	0.35	4150	40
7	2.45	1.57	0.48	4790	47

e2

Intensity		ΔT (°C)		EF (V/m)	
Level	RMS (mA)	Lead	SC	Lead	SC
1	0.35	0.04	0.00	690	3
2	0.70	0.14	0.02	1389	6
3	1.05	0.30	0.05	2088	8
4	1.40	0.54	0.09	2861	12
5	1.75	0.84	0.15	3480	14
6	2.10	1.22	0.22	4190	17
7	2.45	1.65	0.30	4880	19

Figure 3. FEM bioheat predicts temperature increases during Senza HF10 SCS. a. CAD derived human spinal cord model with a Senza HF10 SCS lead placed epidurally in the cervical (c3–c6) spine level (a2a) and in the lower thoracic (T8–T10) spine level (a2b). b. The FEM solution predicted electric field (EF) in the spinal tissues at Senza IPG Level 7 setting (EF rainbow false color, black streamlines showing EF propagation strength). C. Temperature distribution along the spinal cord at Senza IPG Level 7 (temperature heat map) for both c3–c6 (c1) and T8–T12 (c2) spine level. c1a. Inset shows expanded view around energized electrodes (with blue temperature flux lines seeded uniformly at the surface of the stimulating electrode). d. Longitudinal cross section (d1) and transversal cross section (d2) views of temperature distribution in the spinal tissues. (e) Across stimulation intensity (Level 1–7 with corresponding RMS values), ΔT and EF were predicted around the epidural space near electrodes (Lead) and spinal cord (SC). Temperature increased by 0.02°C at the SC and 0.03°C at the lead for Level 1, and by 0.48 °C at the SC and 1.57 °C at the Lead for Level 7 for the cervical spine level, noting these simulations with applied RMS did not account for IPG compliance limitations at higher loads. Temperature increased by 0.00 °C at the SC and 0.04 °C at the lead for Level 1, and by 0.30°C at the SC and 1.65°C at the Lead for Level 7 for the thoracic spine level. [Color figure can be viewed at wileyonlinelibrary.com]

multiple mesh densities refinement contained 17,500,000 and 16,000,000 number of tetrahedral elements, respectively, in the human cervical and thoracic spinal cord models and 458,000 in the phantom model. The final volumetric meshes were imported in COMSOL Multiphysics 5.1 (COMSOL Inc., MA, USA) to computationally solve the model using (bio)-heat multi-physics. The SCS model was solved for active heating (bio-heat with blood perfusion [BPer] and metabolic hear generation [MHG] conditions) whereas the phantom FEM model was solved for passive heating due to joule heat. The baseline temperature gradient for the active heating was predicted by first solving the heat transfer model without stimulation. Both phantom and SCS models were solved under steady-state assumption and the corresponding temperature increases and electric field intensities were predicted. The overall distribution of temperature profile across the tissue compartments were plotted using heat flux and field intensity streamlines (seeded at selected tissue boundaries and proportional in diameter to the logarithm of corresponding magnitudes; Fig. 3).

Bio-Heat Multi-Physics FEM of SCS

Human SCS model was simulated as isotropic homogenous volume conductors. Specifically, we modeled cervical (C3–C6) and lower thoracic (T8-T12) vertebrae levels of the spinal cord. The diameters of the spinal cord were 7.9 (C3–C6) and 7.8 mm (T8–T12) while that of the roots was 0.5 mm for both spine levels. The thicknesses of the adjacent tissues were: CSF, 2.0 mm; dura, 0.2 mm; and epidural space 2.2 mm for the cervical spine level and CSF, 3.2 mm; dura, 0.3 mm; and epidural space 3.2 mm for the lower thoracic spinal level. The Senza HF10 SCS lead was positioned in the epidural space, ~3.3 mm (C3–C6) or 5.1 mm (T8–T12) away from the dorsal surface of the spinal cord, along the mediolateral midline of the spine levels (Fig. 3a). Pennes' bio-heat equation governing joule heating due to stimulation ($\sigma|\nabla V^2|$ where V is potential and σ is conductivity (12,18,19)), metabolic heat generation rate (Q_{met} or *MHG*), and blood perfusion (ω_b *or BPer*) in the spinal tissues was solved to predict temperature increases as mentioned below (20,21):

$$\rho C_p \nabla T = \nabla.(\kappa \nabla T) - \rho_b C_b \omega_b (T - T_b) + Q_{\text{met}} + \sigma \left| \nabla V^2 \right| \quad (5)$$

where, ρ, C_p, T, σ, and κ, respectively, represent tissue density, specific heat, temperature, electrical conductivity, and thermal conductivity. Physical properties of blood such as density (ρ_b=1057 kg/m^3), specific heat (C_b=3600 J/(kg. K)), and temperature (T_b=36.7°C) were assumed constant in all vascular and spinal tissues (vertebrae, epidural space, dura, and spinal cord). *BPer* values were tissue specific and were in the range of 0.0003–0.009 s^{-1} (18,22). Thermal energy is generated in spinal tissues due to local metabolism and enhanced metabolism in response to SCS (23). Blood temperature in the spinal tissues was modeled 0.3°C less than the core spinal cord temperature (37°C) since thermal energy is convectively transported throughout the spinal tissues via blood circulation (19). Metabolic heat generation rate required to balance the initial temperature of spinal cord was calculated using Equation (6) for the range of ω_b, prior to the application of HF10 stimulation as (19,24):

$$Q_{\text{met}} = \rho_b C_b \omega_b (T - T_b) \quad (6)$$

where T is the initial spinal cord temperature and *Tb* is the initial blood temperature. The calculated Q_{met} and the corresponding ω_b values were given as: soft-tissues (Q_{met}, 368 Wm^{-3}; ω_b, 0.00009 s^{-1}), vertebrae (Q_{met}, 21.6 Wm^{-3}; ω_b, 0.00048 s^{-1}), spinal cord and dura (Q_{met}, 15575 Wm^{-3}; ω_b, 0.009 s^{-1}). These balanced Q_{met} values approximated prior experimental measurements (18,22,25).

Unless otherwise states, CSF convection was not modeled. When simulated, CSF was modeled as a Newtonian fluid using the heat transfer in fluids method as described below:

$$\rho C_p \boldsymbol{u}.\nabla T + \nabla.(-\kappa \nabla T) = Q_p \quad (7)$$

where, ρ, C_p, T, $\boldsymbol{u}$, and κ, respectively, represent tissue density, specific heat, temperature, velocity field, and thermal conductivity. Physical properties of CSF such as density (ρ_b=1007 kg/m^3) and specific heat (C_p=4096 J/(kg. K)) were assigned based on values used in previous studies. The velocity field $\boldsymbol{u}$ was assumed uniform and unidirectional (26–28). Macroscopic (large vessel) blood flow was not modeled.

The initial temperature of the tissues was assumed to be 37°C. Thermo-electrical properties of biological tissues were based on aggregated literature values (10,29,30). At kHz frequencies, spinal tissue is considered generally resistive (14,31,32) Intravertebral disc (σ = 0.60 S/m; κ = 0.49 W/(m.K)) and CSF (σ = 1.7S/m; κ = 0.57 W/(m.K)) were modeled avascular, without Q_{met} and ω_b, remaining tissues were perfused and metabolically active as: epidural space (σ = 0.04 S/m; κ = 0.21 W/(m.K), ω_b = 0.00008 s^{-1}, Q_{met} = 302 Wm^{-3}) soft tissues (σ = 0.004 S/m; κ = 0.47 W/(m.K), ω_b = 0. 00009 s^{-1}, Q_{met} = 368 Wm^{-3}), vertebrae (σ = 0. 04 S/m; κ = 0.32 W/(m.K), ω_b = 0. 00048 s^{-1}, Q_{met} = 21.6 Wm^{-3}), dura (σ = 0. 037 S/m; κ = 0.44 W/(m.K), ω_b = 0. 009 s^{-1}, Q_{met} = 15,575 Wm^{-3}), and spinal cord (σ = 0. 1432 S/m; κ = 0.51 W/(m.K), ω_b = 0. 009 s^{-1}, Q_{met} = 15,575 Wm^{-3}).

Heat Phantom FEM

Agarose gel phantom SCS was modeled using the passive heat transfer parameters of Equation (2), excluding biological tissue properties. Parameters of the FEM Phantom model (dimensions, conductivity, and initial temperature) were set based on the experimental measures. The homogenous phantom was modeled with a thermal conductivity (κ) of 0.6 W/(m.K) and electrical conductivities (σ) of 0.025 S/m, 0.04 S/m, and 0.085 S/m, corresponding to the three phantom types fabricated. As in the *in vitro* experiment, we simulated one Senza HF10 SCS lead with eight electrode contacts placed at the center of the agarose gel phantom.

Model Boundary and Initial Conditions

Mimicking clinical montages (bipolar configuration in our study), an inward normal RMS current density (corresponding to the "applied RMS' at each level) was applied across E5 (anode) and E6 (cathode). The electrical conductivities (σ) and thermal conductivities (κ) of the SCS lead (electrode contacts and the inter-electrode material) were set as 4×10^6 S/m and 31 W/(m.K), and 1×10^{-15} S/m and 0.0262 W/(m.K), respectively. Remaining outer boundaries of the human bioheat SCS model and the gel phantom model were electrically insulated. For the thermal boundary conditions, the outer boundaries temperature of both the spinal cord and gel phantom were fixed at a core body temperature (37°C) assuming no convective heat loss to the ambient temperature, no convective gradients across spinal surrounding tissues, and no SCS-induced heating at the model boundaries (22,25,29,30). The unipolar electrode impedance was 1.3 kΩ.

Statistics and Analysis

The statistical distribution of the temperature increases and voltage was tested using Lilliefors corrected K-S statistical test. A one-way

analysis of variance (ANOVA) was used to probe the statistical differences in ΔT across different tested conditions (stimulation intensity, conductivities, and spatial distribution). A critical value (p) < 0.01 was accepted as statistically significant difference between the groups. If significant, a post-hoc multiple comparison Tukey–Kramer's test was used to evaluate differences between the groups.

RESULTS

Our approach was first to characterize the output of the Senza HF10 system IPG, under a range if resistive loads, since this governs power delivered to the leads. IPG limitations were contrasted against a custom bench-to stimulator. Separately, battery run down experiments with resistive loads were used to assess how much energy delivered to the lead contributes to overall energy consumption by the Senza system. Temperature increases around the Senza SCS lead were then measured in custom heat phantom, with varied resistivity phantoms. The data from the phantom was used to verify a heat transfer model. Finally, a bioheat transfer model predicted temperature increases in spinal tissue during Senza HF10 stimulation.

Compliance Voltage and Targeted Current Vs. Output Current

The output voltage, current, and power of the Senza SCS system were quantified under different resistive loads (1–10 kΩ). Output performance was contrasted with a benchtop LCI designed for high-bandwidth and programmed to provide a matched waveform (10 kHz, 30–20–30 μs, symmetric charge balanced biphasic pulses). Intensity was varied on Senza SCS IPG using 1–7 program levels, corresponding to a target amplitude of 1–7 $mA_{peak\text{-}to\text{-}peak}$. The target current indicates a maximal theoretical current. The ideal voltage is the target current times load resistance. The theoretical current RMS and ideal voltage RMS are the RMS of the ideal 10 kHz pulse waveform at the target current or ideal voltage, respectively (see Section Methods).

With a "low" 1 kΩ load (1) and "mid" Level 4/4 $mA_{peak\text{-}to\text{-}peak}$ target intensities, a maximum theoretical voltage of 4 $V_{peak\text{-}to\text{-}peak}$ (2 V_{peak}) was achieved by both Senza SCS and LCI stimulators, though the Senza SCS demonstrated slower rise time resulting in a smoothed waveform (1). With a "high" 10 kΩ load and "mid" Level 4/4 $mA_{peak\text{-}to\text{-}peak}$ target intensity, the LCI stimulator attained a maximal theoretical voltage of 40 $V_{peak\text{-}to\text{-}peak}$ (20 V_{peak}) while the Senza SCS stimulator output peaked at 14.8 V_{peak} (1). With a "high" 10 kΩ load (1) and "high" Level 7/7 $mA_{peak\text{-}to\text{-}peak}$ target intensity, neither stimulator reached the maximal theoretical voltage of 70 $V_{peak\text{-}to\text{-}peak}$ (35 V_{peak}), the Senza SCS system output saturated at 15.6 V_{peak}. The rise slope was faster for the high versus low target current. The Senza SCS IPG provided a 10 kHz symmetric charge balanced biphasic pulses under all conditions tested, but with bandwidth and intensity limitations.

For both Senza SCS (Fig. 1b) and LCI (Fig. 1c) stimulators, stimulator output was measured across various resistive loads (1–10 kΩ) at three target intensities: "low" (1 $mA_{peak\text{-}to\text{-}peak}$, Level 1, with theoretical current RMS 0.39 mA), "mid" (4 $mA_{peak\text{-}to\text{-}peak}$, Level 4 with theoretical current RMS 1.55 mA), and "high" (7 $mA_{peak\text{-}to\text{-}peak}$, Level 7, with theoretical current RMS 2.7 mA). For each intensity and load, the measured current output RMS (1, Senza SCS; 1, LCI) and voltage output RMS (1, Senza SCS; 1, LCI) as a function of theoretical current RMS was determined. For each setting and load, power was calculated as a function of theoretical current RMS (1, Senza SCS; 1, LCI). The maximal theoretical current (RMS) would linearly track theoretical current (RMS) with unit slope, while the ideal theoretical voltage (RMS) would be linear with the theoretical current (RMS), with the slope as the resistive load. Any non-linearity thus represents a deviation from the ideal performance. For the Senza SCS IPG, measured output current tracked the theoretical current up to a 4 kΩ load (1, overlaid lines) whereas for 6–10 kΩ loads, the measured current was significantly lower than the theoretical current, increasingly so for higher theoretical currents ($F_{5,6}$ = 29.07, p < 0.01). For the Senza IPG, voltage output saturated (compliance) at 12 V RMS (15.6 V_{peak}). Peak output current (Fig. 1b1) for the Senza IPG was attenuated when voltage saturation was approached, reflecting both compliance voltage and rise time (1). Calculated Senza IPG output power increased with both theoretical current and stimulation load, as long as compliance voltage was not approached (1). Therefore, at 4–6 kΩ loads, a maximum power was achievable, with delivered power decreasing for both lower or higher loads. Qualitatively, similar behavior was observed for LCI stimulator measured current (1), voltage (1), and power (1) but reflecting higher relative compliance voltage and bandwidth (pulse rise rate). The measured currents for each stimulation level (Level 1–7) under a 1 kΩ load were considered "applied RMS" values for subsequent FEM simulations.

Battery Rundown

The IPG battery complete reported drainage time, $T_{Drainage}$ (sec) were 189,864, 306,000, 71,190, 140,760, 71,700, and 102,942, respectively, for Level 7 at 1 kΩ, Level 4 at 1 kΩ, Level 7 at 6 kΩ, Level 4 at 6 kΩ, Level 7 at 10 kΩ, and Level 4 at 10 kΩ. The rank order of increasing drainage time corresponded with rank order of decreasing power deposition; notably, run time was shorter for Level 7 at 6 kΩ than any other condition including Level 7 at 10 kΩ. Baseline power consumption ($P_{Baseline}$) was estimated at 0.0024 W. Total energy delivery to the lead (E_{Lead}) is calculated as 1317 J, 691 J, 1259 J, 1380 J, 939 J, and 1159 J, respectively, for Level 7 at 1 kΩ, Level 4 at 1 kΩ, Level 7 at 6 kΩ, Level 4 at 6 kΩ, Level 7 at 10 kΩ, and Level 4 at 10 kΩ. Averaged across conditions, the estimated depletion energy of the IGP (E_{Th}) is 1479 ± 100 J when the battery is fully drained.

Temperature Increases in SCS Heat Phantom

Temperature increases around the Senza SCS lead across stimulation intensities were measured in the heat phantom (Table 1). We considered three phantom electrical conductivities: 0.025, 0.04, and 0.085 S/m. ΔT was significantly higher in the lower conductivity phantom ($F_{1,46}$ = 39.19, p < 0.01). At the maximum tested stimulation intensity (Level 7, 2.5 mA applied RMS), the maximum ΔT were 0.84°C, 0.74°C, and 0.39°C for 0.25, 0.04, and 0.085 S/m phantom conductivity, respectively. Temperature was also predicted by the heat phantom based on applied RMS (values in brackets, (Table 1). Note that target current may not be achieved in the lower conductivity (0.25 S/m) phantom, reflecting a measured temperature increase below that predicted (Table 1). The time constant (τ) for temperature increases (time for 63% of the maximum ΔT) did not differ significantly across conditions tested (mean 1.88 ± 0.16 min; $F_{2,9}$ = 0.2, p > 0.01). Temperature increase and time constant did not differ significantly ($F_{1,46}$ = 0, p > 0.01) across tested electrode contact pairs.

In a medium conductivity phantom (0.04 S/m), temperature increases with Senza HF10 IPG stimulation intensity (1–7 level) ($F_{6,18}$ = 322.33, p < .01). To further verify the dependence of temperature rise on RMS intensities, irrespective of waveform details, we applied a 10 kHz sinusoidal stimulation using the LCI stimulator, which resulted in a comparable temperature increase for matched RMS (Fig. 2b). Temperature increases supralinearly with RMS/level.

Table 1. Significant Temperature Increases in a Heat Phantom During Senza HF10 SCS Stimulation.

		Electrodes/Levels Combinations			
		E5–E6/Level 4	E5–E6/Level 7	E1–E2/Level 4	E1–E2/Level 7
Phantom conductivity (S/m)	0.025	*	*	*	*
		0.39 ± 0.01 [0.49]°C	0.84 ± 0.02 [1.50]°C	0.39 ± 0.02°C	0.82 ± 0.02°C
		2.03 ± 0.12 min	1.87 ± 0.1 min		
	0.040	*	*	*	*
		0.25 ± 0.02 [0.31]°C	0.74 ± 0.06 [0.93]°C	0.26 ± 0.03°C	0.76 ± 0.06 C
		1.96 ± 0.11 min	1.73 ± 0.08 min		
	0.085		*		*
		0.14 ± 0.02 [0.14]°C	0.39 ± 0.01 [0.44]°C	0.12 ± 0.02°C	0.41 ± 0.02°C
		2.00 ± 0.03 min	1.67 ± 0.4 min		

Temperature increases by Senza HF10 system in a heat phantom experiment (mean ± SD) and FEM prediction (FEM) at Level 4 (1.39 mA RMS; gray columns) and Level 7 (2.45 mA RMS, in low (0.025 S/m), medium (0.04 S/m), and high conductivity (0.085 S/m) phantoms, using two adjacent bipole electrode combinations (E1 and E2; E5 and E6). Temperature measurements were similar in both tested electrode combinations with ΔT at Level 7 of ~0.82°C, ~0.75°C, and ~0.40°C in low, medium, and high conductivity phantom, respectively. The FEM simulation was based on the IPG applied RMS across 1 kΩ. However, IPG compliance limitations can further reduce output at increasing loads (Fig. 1). Consistent with this, especially with increasing level and phantom resistance, FEM simulations predicted significantly higher (*) temperature increase than measured experimentally. In a sense, Senza HF10 IPG output limits dampen resulting temperature increases. Temperature rise time did not vary significantly across stimulation intensities or media conductivities ($p > 0.01$).

*ΔT predicted by FEM is significantly higher than experimental measurements. [ ] FEM simulation of applied RMS 1 kΩ (not emulating increased bandwith limits at high load).

Temperature increases predicted by the FEM heat model (RMS boundary condition, see Section Methods) correlated with the experimental measurements in the HP34 gel phantom across tested conditions ($R^2 = 0.88$, $F_{3,18} = 167.39$, $p < 0.01$, Fig. 2b). The percent differences between FEM predicted ΔTs and the experimental ΔTs for level 1–7 are 1.2, 2.3, 2.8, 6.5, 13.2, 14.5, and 18.8% and 1.2, 2.1, 3.1, 5.3, 13.3, 13.7, and 17.5%, respectively, for Senza IPG and LCI.

Senza HF10 SCS Bioheat Model Prediction

Temperature increases and field intensities around the SCS lead (epidural space) and at the spinal cord during Senza HF10 SCS were predicted by the human spinal cord bio-heat model (Fig. 3). For the cervical model, predicted ΔTs at the lead and spinal cord for Level 1 (minimum) and Level 7 (maximum) were 0.03°C (Level 1) and 1.57°C (Level 7) at the lead, and 0.02°C (Level 1) and 0.48°C (Level 7) at the spinal cord (SC). For the lower thoracic SCS model, predicted ΔTs for Level 1 and Level 7 were 0.04 °C (Level 1) and 1.65 °C (Level 7) at the Lead, and 0.00 °C (Level 1) and 0.30 °C (Level 7) at the spinal cord (SC). Heating increased supralinearly with RMS intensities (doubling stimulation level doubles RMS and increases temperature rise by >twofold (Fig. 3c,d) (10). While, as expected, the field intensity (EF) increased linearly with the RMS intensities (cervical segment: 700 V/m at the lead and 7 V/m at the SC at Level 1; 4790 V/m at the lead and 47 V/m at the SC at Level 7; Fig. 3b,e1; Thoracic segment: 690 and 3 V/m, respectively at the lead and at the SC at Level 1; 4880 V/m and 19 V/m, respectively, at the SC at Level 7; Fig. 3b,e2). When CSF flow is taken into account, for the lower thoracic SCS, at Level 7, predicted ΔTs at the lead and spinal cord were 1.61 and 0.23 °C, respectively.

DISCUSSION

We previously proposed a general MoA for kHz SCS based on waveform pulse-compression leading to tissue joule heating (Fig. 4) (10). Here we report a temperature increases around the Senza HF10 SCS system leads that develop in a manner predictable based on IPG performance, program level, and load impedance (Table 1; Fig. 2b). Maximal temperature rise occurs when stimulation intensity and load impedance are increased, until Senza HF10 IPG compliance voltage is reached (Fig. 1). Importantly, even before Senza HF10 IPG voltage compliance is reached, Senza IPG bandwidth limitations reduce output RMS (Fig. 1). Notwithstanding dampening of Senza IPG output, tissue heating increases supralinearly with stimulation level (in contrast to linear electric field).

The time constant (τ) of heating is in the order of minutes (Table 1), with potential neurophysiological consequences of heating developing over longer periods of time. A temperature-based MOA for kHz SCS may therefore, explain the slow wash-in and wash-out times of clinical outcomes (33–37). In contrast to transient temperature changes produced by physical activity and environmental factors (10), heating produced by kHz SCS is chronic, consistent with a MoA that follow a slow time-course. It is established that a range of neurophysiological processes at the spinal cord would be sensitive to temperature rises in the range of 0.5°C (10,38–40), especially over long term exposure (e.g., chronic stimulation). Alongside validating temperature increase *in vivo*, it remains to be studied which temperature-dependent cascades (e.g., heat shock protein, perfusion, ion-channel expression) would determine kHz SCS clinical outcomes. Establishing the degree of temperature change, the focus of the present study, is a prerequisite first step to isolating the functional consequences if kHz SCS heating.

Given that electric field spatial profile and temperature field spatial profiles are distinct, a temperature-based MoA would suggest distinct optimization (programming) strategies (10). The dependence of temperature increases only on waveform RMS (e.g., two waveforms with distinct frequency and pulse shape but matched RMS will produce the same heating), so if validated, a temperature-based MoA has implications for kHz SCS implementation (10).

Based on resistive-load testing and IPG waveforms tested, the energy delivered to the lead (into the body) represents 47–94% of total IPG battery energy usage, reducing battery life accordingly. For conditions tested, instant power to the lead was 0.9 – 7× of

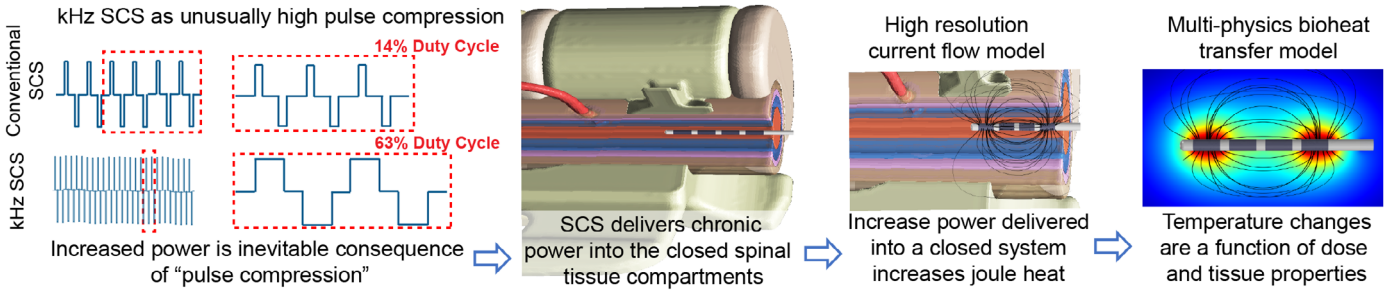

Figure 4. Biophysics of a temperature-based MoA for kHz SCS. (left to right) kHz SCS has high power as a result of increasing duty cycle (pulse compression). IPG hardware specific bandwidth and compliance may limit actual delivered power. kHz SCS energy is providing continuously (chronically) into the enclosed intravertebral space such that temperature will rise without limit in the absence of passive and active heat clearance. The resulting temperature changes are therefore a function of stimulation dose and tissue properties. Should temperature increases be validated in vivo as a MoA of kHz SCS, here, we show how quantification of IPG characteristics and bioheat models allows prediction and optimization of temperature changes. [Color figure can be viewed at wileyonlinelibrary.com]

background IPG consumption; all the more notable given the size of the energized electrodes (0.12 cm^2) compared to the IPG can surface (48.24 cm^2).

The bioheat models of kHz SCS remain to be validated, but supralinear dependence of heating on only waveform RMS follows established physics of joule heat (8); and was verified in heat phantoms (Fig. 2). Bioheat models have proven reliable based on thermographic measurement for other device types (41,42). Thermographic measurement in an appropriate SCS animal model would support a heating MoA for kHz SCS; though to be translationally meaningful for this purpose animal model should approximate clinical heat deposition. Various factors may either accentuate (e.g., stimulus activated metabolic activity) or dampen (e.g., heat convection by CSF and macroscopic blood flow) temperature increases. Notably, the very waveform factors (pulse compression) that make kHz SCS, inefficient based on conventional neuronal activation MoA (7), make kHz SCS optimized for heating. It is precisely because all biophysical process (e.g., molecular synaptic, vascular, neuronal excitability; (17,22,43,44)) are sensitive to temperature, that the proposal for a heating-based MoA for kHz SCS requires ongoing investigation.

Authorship Statement

Adantchede L Zannou designed the work, acquired and analyzed data, and drafted the manuscript. Niranjan Khadka designed the work, analyzed data, and edited the manuscript. Mohamad FallahRad acquired data, edited, and reviewed the manuscript. Dennis Q. Truong analyzed data, edited, and critically reviewed the manuscript. Brian H. Kopell reviewed the manuscript and provided critical intellectual content. Marom Bikson designed the work, drafted the manuscript, and revised it for important intellectual content.

How to Cite this Article:

Zannou A.L., Khadka N., FallahRad M., Truong D.Q., Kopell B.H., Bikson M. 2019. Tissue Temperature Increases by a 10 kHz Spinal Cord Stimulation System: Phantom and Bioheat Model.
Neuromodulation 2019; E-pub ahead of print. DOI:10.1111/ner.12980

REFERENCES

1. Kapural L, Yu C, Doust MW et al. Comparison of 10-kHz high-frequency and traditional low-frequency spinal cord stimulation for the treatment of chronic Back and leg pain: 24-month results from a multicenter, randomized, controlled pivotal trial. *Neurosurgery* 2016;79:667–677.
2. Mendell LM. Constructing and deconstructing the gate theory of pain. *Pain* 2014; 155:210–216.
3. Zhang TC, Janik JJ, Grill WM. Mechanisms and models of spinal cord stimulation for the treatment of neuropathic pain. *Brain Res* 2014;1569:19–31.
4. Lempka SF, McIntyre CC, Kilgore KL, Machado AG. Computational analysis of kilohertz frequency spinal cord stimulation for chronic pain management. *Anesthesiology* 2015;122:1362–1376.
5. Maeda Y, Ikeuchi M, Wacnik P, Sluka KA. Increased c-fos immunoreactivity in the spinal cord and brain following spinal cord stimulation is frequency-dependent. *Brain Res* 2009;1259:40–50.
6. Crosby ND, Janik JJ, Grill WM. Modulation of activity and conduction in single dorsal column axons by kilohertz-frequency spinal cord stimulation. *J Neurophysiol* 2017; 117:136–147.
7. Song Z, Viisanen H, Meyerson BA, Pertovaara A, Linderoth B. Efficacy of kilohertz-frequency and conventional spinal cord stimulation in rat models of different pain conditions. *Neuromodulation J Int Neuromodulation Soc* 2014;17:226–234. discussion 234-235.
8. Chakraborty D, Truong DQ, Bikson M, Kaphzan H. Neuromodulation of axon terminals. *Cereb Cortex* 2018;28:2786–2794.
9. Bikson M, Inoue M, Akiyama H et al. Effects of uniform extracellular DC electric fields on excitability in rat hippocampal slices in vitro. *J Physiol* 2004;557:175–190.
10. Zannou AL, Khadka N, Truong DQ et al. Temperature increases by kilohertz frequency spinal cord stimulation. *Brain Stimulat* 2018;12:62–72. http://www.sciencedirect.com/science/article/pii/S1935861X1830353X.
11. Elwassif MM, Datta A, Rahman A, Bikson M. Temperature control at DBS electrodes using heat sink: Experimentally validated FEM model of DBS lead architecture. *J Neural Eng* 2012;9:046009.
12. Elwassif MM, Kong Q, Vazquez M, Bikson M. Bio-heat transfer model of deep brain stimulation induced temperature changes. In*: 2006 International Conference of the IEEE Engineering in Medicine and Biology Society*, 2006:3580–3.
13. Abejon D, Feler CA. Is impedance a parameter to be taken into account in spinal cord stimulation? *Pain Physician* 2007;10:533–540.
14. Utz M, Miller JW, Reddy CG et al. In vivo measurements of the frequency-dependent impedance of the spinal cord. *bioRxiv* 2018;1–33. http://dx.doi.org/10.1101/252965.
15. Schade CM, Schultz DM, Tamayo N, Iyer S, Panken E. Automatic adaptation of neurostimulation therapy in response to changes in patient position: Results of the posture responsive spinal cord stimulation (PRS) research study. *Pain Physician* 2011;14:407–417.
16. Kameyama T, Hashizume Y, Sobue G. Morphologic features of the normal human cadaveric spinal cord. *Spine* 1996;21:1285–1290.
17. Baysal U, Haueisen J. Use of a priori information in estimating tissue resistivities—application to human data in vivo. *Physiol Meas* 2004;25:737–748.
18. Collins CM, Smith MB. Turner R. model of local temperature changes in brain upon functional activation. *J Appl Physiol* 2004;97:2051–2055.
19. Hodson DA, Barbenel JC, Eason G. Modelling transient heat transfer through the skin and a contact material. *Phys Med Biol* 1989;34:1493–1507.
20. Chang I. Finite element analysis of hepatic radiofrequency ablation probes using temperature-dependent electrical conductivity. *Biomed Eng Online* 2003;2:12.
21. Tungjitkusolmun S, Woo EJ, Cao H, Tsai JZ, Vorperian VR, Webster JG. Finite element analyses of uniform current density electrodes for radio-frequency cardiac ablation. *IEEE Trans Biomed Eng* 2000;47:32–40.
22. Xu X, Tikuisis P, Giesbrecht G. A mathematical model for human brain cooling during cold-water near-drowning. *J Appl Physiol* 1999;86:265–272.
23. Morrison SF, Nakamura K. Central neural pathways for thermoregulation. *Front Biosci J Virtual Libr* 2011;16:74–104.

24. Wilson SB, Spence VA. A tissue heat transfer model for relating dynamic skin temperature changes to physiological parameters. *Phys Med Biol* 1988;33:895–912.
25. Fiala D, Lomas KJ, Stohrer M. A computer model of human thermoregulation for a wide range of environmental conditions: The passive system. *J Appl Physiol* 1999;87:1957–1972.
26. Linninger AA, Xenos M, Zhu DC, Somayaji MR, Kondapalli S, Penn RD. Cerebrospinal fluid flow in the Normal and hydrocephalic human brain. *IEEE Trans Biomed Eng* 2007;54:291–302.
27. Yan L. Quantitative analysis of intraspinal cerebrospinal fluid flow in normal adults. http://www.nrronline.org/article.asp?issn=1673-5374;year=2012;volume=7;issue=15;spage=1164;epage=1169;aulast=Yan
28. Smith KD, Zhu L. Theoretical evaluation of a simple cooling pad for inducing hypothermia in the spinal cord following traumatic injury. *Med Biol Eng Comput* 2010;48:167–175.
29. Gabriel S, Lau RW, Gabriel C. The dielectric properties of biological tissues: II. Measurements in the frequency range 10 Hz to 20 GHz. *Phys Med Biol* 1996;41:2251–2269.
30. IT'IS Foundation. Tissue Properties Database V3.0. IT'IS Foundation; 2015. http://www.itis.ethz.ch/db3-0
31. Gabriel C, Peyman A, Grant EH. Electrical conductivity of tissue at frequencies below 1 MHz. *Phys Med Biol* 2009;54:4863–4878.
32. Bossetti CA, Birdno MJ, Grill WM. Analysis of the quasi-static approximation for calculating potentials generated by neural stimulation. *J Neural Eng* 2008;5:44–53.
33. Sdrulla AD, Guan Y, Raja SN. Spinal cord stimulation: Clinical efficacy and potential mechanisms. *Pain Pract* 2018;18:1048–1067.
34. Chakravarthy K, Richter H, Christo PJ, Williams K, Guan Y. Spinal cord stimulation for treating chronic pain: Reviewing preclinical and clinical data on paresthesia-free high-frequency therapy. *Neuromodulation Technol Neural Interface* 2018;21:10–18.
35. Shechter R, Yang F, Xu Q et al. Conventional and kilohertz-frequency spinal cord stimulation produces intensity- and frequency-dependent inhibition of mechanical hypersensitivity in a rat model of neuropathic pain. *Anesthesiol J Am Soc Anesthesiol* 2013;119:422–432.
36. Kilgore KL, Bhadra N. Nerve conduction block utilising high-frequency alternating current. *Med Biol Eng Comput* 2004;42:394–406.
37. Li S, Farber JP, Linderoth B, Chen J, Foreman RD. Spinal cord stimulation with "conventional clinical" and higher frequencies on activity and responses of spinal neurons to noxious stimuli: An animal study. *Neuromodulation Technol Neural Interface* 2018;21:440–447.
38. Masuda H, Hirata A, Kawai H et al. Local exposure of the rat cortex to radiofrequency electromagnetic fields increases local cerebral blood flow along with temperature. *J Appl Physiol* 2011;110:142–148.
39. Kiyatkin EA, Brown PL, Wise RA. Brain temperature fluctuation: A reflection of functional neural activation. *Eur J Neurosci* 2002;16:164–168.
40. LaManna JC, McCracken KA, Patil M, Prohaska OJ. Stimulus-activated changes in brain tissue temperature in the anesthetized rat. *Metab Brain Dis* 1989;4:225–237.
41. Kim S, Tathireddy P, Normann RA, Solzbacher F. in vitro and in vivo study of temperature increases in the brain due to a neural implant. In: *2007 3rd International IEEE/EMBS Conference on Neural Engineering*. 2007. 163–6.
42. Vrba J, Janca R, Blaha M et al. Modeling of brain tissue heating caused by direct cortical stimulation for assessing the risk of thermal damage. *IEEE Trans Neural Syst Rehabil Eng Publ IEEE Eng Med Biol Soc* 2019;27:440–449.
43. Steffens HJ. *James Prescott Joule and the concept of energy Dawson Science History Publications*; 1979.
44. Moser E, Mathiesen I, Andersen P. Association between brain temperature and dentate field potentials in exploring and swimming rats. *Science* 1993;259:1324–1326.

